arXiv:1608.07873v1 [cond-mat.mes-hall] 29 Aug 2016

Finite-Size Scaling Analysis of the Conductivity of Dirac Electrons on a Surface of Disordered Topological Insulators

Yositake Takane

Department of Quantum Matter, Graduate School of Advanced Sciences of Matter, Hiroshima University, Higashihiroshima, Hiroshima 739-8530, Japan

(Received)

Two-dimensional (2D) massless Dirac electrons appear on a surface of three-dimensional topological insulators. The conductivity of such a 2D Dirac electron system is studied for strong topological insulators in the case of the Fermi level being located at the Dirac point. The average conductivity $\langle\sigma\rangle$ is numerically calculated for a system of length L and width W under the periodic or antiperiodic boundary condition in the transverse direction, and its behavior is analyzed by applying a finite-size scaling approach. It is shown that $\langle\sigma\rangle$ is minimized at the clean limit, where it becomes scale-invariant and depends only on L/W and the boundary condition. It is also shown that once disorder is introduced, $\langle\sigma\rangle$ monotonically increases with increasing L. Hence, the system becomes a perfect metal in the limit of $L \to \infty$ except at the clean limit, which should be identified as an unstable fixed point. Although the scaling curve of $\langle\sigma\rangle$ strongly depends on L/W and the boundary condition near the unstable fixed point, it becomes almost independent of them with increasing $\langle\sigma\rangle$, implying that it asymptotically obeys a universal law.

1. Introduction

Three-dimensional topological insulators host low-energy electron states on their surfaces.[1–4] These surface electrons are called Dirac electrons as they obey a massless Dirac equation and hence possess a linear energy dispersion forming a gapless conic structure (i.e., a Dirac cone) in the reciprocal space. Topological insulators are classified into either strong topological insulators (STIs) or weak topological insulators (WTIs). The behavior of Dirac electrons is different for these two insulators. Dirac electrons appear on every surface of an STI, while they appear only on side surfaces in a typical WTI. Another important difference is that an STI typically has one Dirac cone, while a WTI has two Dirac cones.

Let us consider electron transport on a surface of topological insulators in the presence of disorder, focusing on the STI case in which surface electrons constitute a two-dimensional (2D) disordered Dirac electron system with one Dirac cone. The system under consideration is essentially equivalent to graphene in the presence of only long-range impurities, which do not induce intervalley scattering.[5] Thus, to consider electron transport on a surface of STIs, we can utilize theoretical results for graphene[5–14] in addition to those of studies focused on topological insulators.[15–19] An important question is whether the system exhibits a metal-insulator transition. The simplest way to answer this question is to analyze the behavior of the average conductivity by using a finite-size scaling approach.[20] Such studies have been reported in Refs. 10 and 12. It is demonstrated that the system shows no metal-insulator transition and becomes a perfect metal in the thermodynamic limit. This is in marked contrast to the case of ordinary 2D electron systems with time-reversal symmetry and strong spin-orbit interaction.[21–23]

However, there are subtle issues that need further studies. In the scaling analysis of disordered graphene under a two-terminal setup,[10] the periodic boundary condition (PBC) is imposed in the transverse direction of the 2D Dirac electron system. In realistic samples of an STI, the antiperiodic boundary condition (ABC) should be imposed to correctly take account of a Berry phase π due to spin-to-surface locking.[24–28] The PBC applies when an external π magnetic flux pierces the system in the longitudinal direction without touching surface states. Note that the excitation spectrum of the system changes according to whether the PBC or the ABC is imposed. Under the PBC, the system has gapless excitations, while it acquires a finite-size gap under the ABC. It has been shown that one perfectly conducting channel is stabilized in the PBC case, while such a special channel does not appear in the ABC case. A perfectly conducting channel transmits electrons from one end of the system to the other without backscattering.[29–37] We expect that its effect on electron transport depends on whether the width W of the system is larger or smaller than its length L. The influence of a perfectly conducting channel should be smeared if $W \gg L$, and hence many conducting channels open at the Fermi level. However, if $L \gg W$, it should dominate electron transport properties. Is the boundary condition as well as the aspect ratio L/W completely irrelevant in a finite-size scaling analysis?

Electron transport in the presence of disorder has also been examined in the WTI case.[38–41] Dirac electrons on

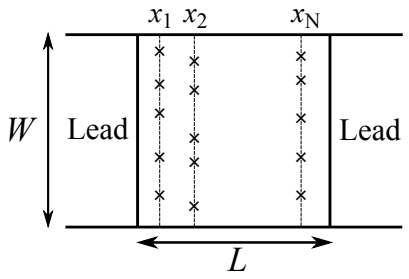

Fig. 1. Structure of a 2D sample of length L and width W considered in the text, where crosses represent impurities. The role of the dashed lines is explained at the end of Sect. 2.

a side surface of WTIs are described by a 2D chain model[40–43] consisting of one-dimensional helical channels, each of which is coupled with its nearest neighbors. The number of helical channels plays an important role; if it is odd, the system has gapless excitations, while it acquires a finite-size gap if it is even.[38,44] Accordingly, the presence or absence of a perfectly conducting channel is determined by this parity.[38,41,45] Hence, the parity of the channel number plays a role similar to that of the boundary condition in the STI case. The finite-size scaling analysis that takes account of the parity effect[41] suggests that this affects the scaling curve of the average conductivity near the clean limit.

In this paper, we numerically study the behavior of the average conductivity $\langle\sigma\rangle$ in a disordered 2D Dirac electron system with a single Dirac cone of length L and width W, focusing on the effects of the transverse boundary condition and the aspect ratio $R \equiv L/W$. Our attention is restricted to the case of the Fermi level being located at the Dirac point, where $\langle\sigma\rangle$ is expected to be minimized.[5,6] We numerically calculate $\langle\sigma\rangle$ for the system with a fixed R under the PBC or the ABC, and analyze its behavior using a finite-size scaling approach. It is shown that $\langle\sigma\rangle$ is minimized at the clean limit, where it becomes scale-invariant and depends only on R and the boundary condition. It is also shown that $\langle\sigma\rangle$ monotonically increases with increasing L in the presence of disorder. From these results, we conclude that the system becomes a perfect metal in the limit of $L \to \infty$ except at the clean limit, which should be identified as an unstable fixed point. The scaling curve of $\langle\sigma\rangle$ depends on R and the boundary condition (i.e., the presence/absence of a finite-size gap) near the unstable fixed point. However, it becomes almost independent of them with increasing $\langle\sigma\rangle$, implying that it asymptotically obeys a universal law. We set $\hbar = 1$ throughout this paper.

2. Model and Formulation

Let us consider a disordered 2D Dirac electron system of width W in the y-direction being infinitely long in the x-direction (see Fig. 1). We impose either the PBC or the ABC in the y-direction. The region of $L \geq x \geq 0$ is regarded as the sample with disorder, and the region of $x < 0$ ($x > L$) plays the role of the left (right) lead. We adopt the following Dirac Hamiltonian:

$$H = v \begin{bmatrix} -i\partial_x + V(x,y) & -\partial_y \\ \partial_y & i\partial_x + V(x,y) \end{bmatrix} \quad (1)$$

with $V(x,y) \equiv V_{\rm imp}(x,y) + U(x)$. Here, $V_{\rm imp}(x,y)$ represents the disorder potential arising from random impurities, while $U(x)$ is included to simulate the setup[46] in which the Fermi level is fixed at the Dirac point ($\epsilon = 0$) in the sample region, while the left and right leads are deeply doped. Accordingly, we set $U(x) = 0$ for $L > x > 0$, and otherwise $U(x) = -U_0$ with U_0 being positive and large. Let us briefly describe the wave functions at an energy ϵ in the case of $V(x,y) \equiv 0$. The transverse function is given by

$$\chi_m(y) = \frac{1}{\sqrt{W}} e^{iq_m y} \begin{bmatrix} a_m^{\pm} \\ b_m^{\pm} \end{bmatrix}, \quad (2)$$

where $q_m = 2\pi m/W$ and

$$\begin{bmatrix} a_m^{\pm} \\ b_m^{\pm} \end{bmatrix} = \frac{1}{\sqrt{|\pm k_m - \frac{\epsilon}{v}|^2 + q_m^2}} \begin{bmatrix} iq_m \\ \pm k_m - \frac{\epsilon}{v} \end{bmatrix}. \quad (3)$$

Here, m is given by

$$m = 0, \pm 1, \pm 2, \ldots \quad (4)$$

in the PBC case and

$$m = \pm\frac{1}{2}, \pm\frac{3}{2}, \pm\frac{5}{2}, \cdots \quad (5)$$

in the ABC case. For the mth mode, the dispersion relation as a function of the longitudinal wave number k is $\epsilon_m(k) = \pm v\sqrt{k^2 + q_m^2}$. In the PBC case, q_m vanishes for $m = 0$, indicating that the system has gapless excitations, while $m = 0$ is not allowed in the ABC case so a finite-size gap opens across the Dirac point. If $|\epsilon| > v|q_m|$, the mth mode provides two counterpropagating channels. The corresponding wave functions are

$$\varphi_m^{\pm}(x,y) = \frac{1}{\sqrt{v_m}} \chi_m(y) e^{\pm i k_m x}, \quad (6)$$

where $\pm$ specifies the propagating direction, $k_m = \sqrt{(\epsilon/v)^2 - q_m^2}$, and the group velocity v_m is obtained as $v_m = v(vk_m/|\epsilon|)$. If $|\epsilon| < v|q_m|$, the mth mode provides two evanescent channels. The corresponding wave functions are obtained from Eq. (6) by the replacement of k_m with $i\kappa_m$, where $\kappa_m = \sqrt{q_m^2 - (\epsilon/v)^2}$. The group velocity has no physical meaning for evanescent channels. The number of modes should be restricted to a finite number M in actual numerical calculations. We set M be an odd (even) integer in the PBC (ABC) case, and then restrict m as $m_{\rm max} \geq m \geq -m_{\rm max}$ with

$$m_{\rm max} = \frac{M-1}{2}. \quad (7)$$

Here, we define the short length scale a by $a \equiv W/M$, which is on the order of the spatial resolution of plane

waves limited by the restriction of transverse modes. This is equivalent to saying that W is an integer multiple of a,

$$M \equiv W/a. \tag{8}$$

We also assume that L is an integer multiple of a and set

$$N \equiv L/a. \tag{9}$$

The disorder potential $V_{\rm imp}(x,y)$ is assumed to consist of δ-function-type impurities in the sample region,

$$V_{\rm imp}(x,y) = \sum_{p=1}^{N_{\rm imp}} V_p a^2 \delta(x-x_p)\delta(y-y_p), \tag{10}$$

where V_p is the strength of the pth impurity located at $(x,y)=(x_p,y_p)$ and $N_{\rm imp}$ is the total number of impurities. We define γ in terms of the correlation function of $V_{\rm imp}(x,y)$ as[7]

$$\gamma = \frac{1}{v^2}\int_0^L dx' \int_0^W dy' \langle V_{\rm imp}(x,y) V_{\rm imp}(x',y')\rangle, \tag{11}$$

where $\langle\cdots\rangle$ represents the disorder average. If V_p is assumed to be uniformly distributed within the interval of $[-V_0,+V_0]$, we find that $\gamma = (1/3)\Gamma$ with

$$\Gamma = \left(\frac{a}{v}\right)^2 \frac{a^2}{LW} N_{\rm imp} V_0^2. \tag{12}$$

We use Γ to characterize the strength of disorder.

The dimensionless conductance g of a sample with impurities is determined by the Landauer formula,

$$g = {\rm tr}\{\boldsymbol{t}^\dagger \boldsymbol{t}\}, \tag{13}$$

where $\boldsymbol{t}$ is the transmission matrix. As the area of the sample is $W \times L$, the dimensionless conductivity σ is given by

$$\sigma = \frac{L}{W} g. \tag{14}$$

The transmission matrix for a given impurity configuration is numerically determined by using the method presented in Ref. 47. In this method, the S matrix for the whole system is decomposed into single-impurity parts and free-propagating parts. Once they are evaluated, we can construct the S matrix using a composition law. If the above method is straightforwardly applied to our system, the number of single-impurity parts is $N_{\rm imp}$ and that of free-propagating parts is $N_{\rm imp}+1$. In actual numerical calculations, we set $N_{\rm imp} = N \times M$. To save computational time, we employ the following procedure (see Fig. 1):[41] randomly choose N points on the x-axis in the sample region such that $L > x_N > \cdots > x_2 > x_1 > 0$ and then randomly place M impurities on each line of width W at $x = x_i$ $(i = 1, 2, \ldots, N)$. With this procedure, the number of single-impurity parts is reduced to N while the total number of impurities is $N_{\rm imp} = N \times M$.

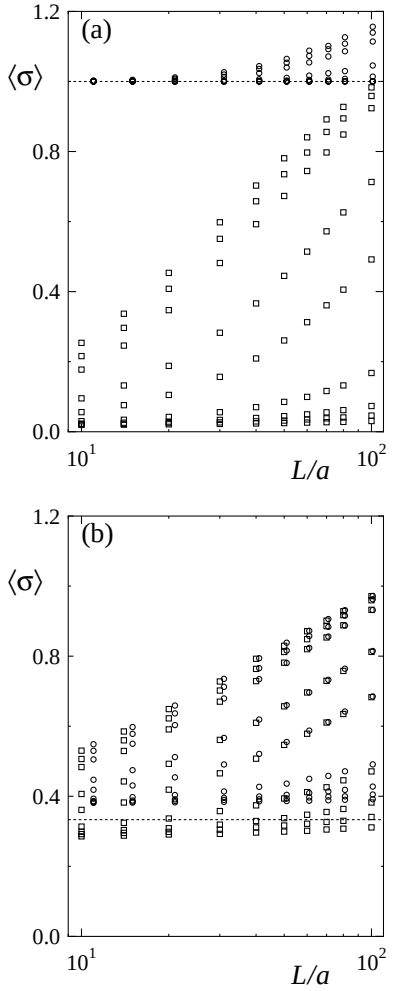

Fig. 2. Average conductivity in the cases of (a) $R = 1$ and (b) $R = 1/3$ as functions of L/a for $\Gamma = 0.6$, 0.7, 0.8, 1.0, 1.5, 2.0, 3.0, 3.5, and 4.0 from bottom to top. Circles and squares respectively correspond to the PBC case and the ABC case. Dotted lines designate $\langle\sigma\rangle = 1$ in (a) and $\langle\sigma\rangle = 1/3$ in (b).

3. Numerical Results

Now, we present the numerical results of the average conductivity $\langle\sigma\rangle$ for various system sizes with a fixed aspect ratio $R \equiv N/M$. We particularly consider the two cases of $R = 1$ and $R = 1/3$. In the case of $R = 1$, the system size is varied from $N \times M = 11 \times 11$ to 201×201 in the PBC case and from 10×10 to 200×200 in the ABC case. In the case of $R = 1/3$, the system size is varied from $N \times M = 11 \times 33$ to 141×423 in the PBC case and from 10×30 to 140×420 in the ABC case. As the number of impurities is fixed at $N_{\rm imp} = N \times M$, the strength of disorder is simply expressed as $\Gamma = (a/v)^2 V_0^2$. This value is tuned within $\Gamma = 0.6$–4.0 by adjusting V_0. Actually, we examine the cases with $\Gamma = 0.6$, 0.7, 0.8, 1.0, 1.5, 2.0, 3.0, 3.5, and 4.0. When performing the ensemble average, the number of samples, $N_{\rm sam}$, is set larger than 5000 so that the relative uncertainty $\Delta\sigma/\langle\sigma\rangle$ is smaller than 0.005 at

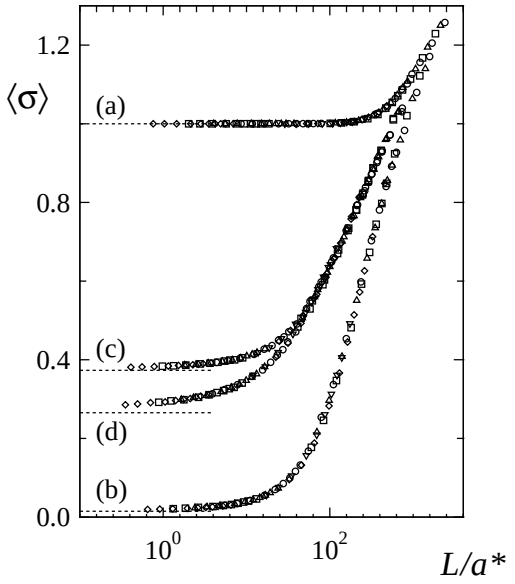

Fig. 3. One-parameter scaling plot of the average conductivity for (a) the case with $R = 1$ under the PBC, (b) that under the ABC, (c) the case with $R = 1/3$ under the PBC, and (d) that under the ABC. Here, the data sets for $\Gamma = 0.6$, 0.7, 0.8, 1.0, 1.5, 2.0, 3.0, 3.5, and 4.0 are used. Dotted lines indicate the clean-limit values of the conductivity (see the text).

each data point, where $\Delta\sigma \equiv (\mathrm{var}\{\sigma\}/N_{\mathrm{sam}})^{1/2}$.

The L dependence of $\langle\sigma\rangle$ is shown in Fig. 2 within the interval of $101 \geq L/a \geq 10$. Clearly, $\langle\sigma\rangle$ increases with increasing Γ, and it also increases with increasing L although the rate of increase becomes very small at small Γ. We observe that $\langle\sigma\rangle$ behaves differently depending on R and/or the boundary condition. Hence, the following four cases are separately considered below: the cases of $R = 1$ under the PBC and the ABC, and the cases of $R = 1/3$ under the PBC and the ABC. Notably, $\langle\sigma\rangle$ is always larger than unity in the case of $R = 1$ under the PBC [see Fig. 2(a)], which results from the fact that one perfectly conducting channel is stabilized under the PBC. The presence of a perfectly conducting channel ensures that $\langle g\rangle > 1$, and this directly accounts for the behavior since $\langle\sigma\rangle = \langle g\rangle$ in this case. In the case of $R = 1/3$ under the PBC, the average conductivity is also bounded below as $\langle\sigma\rangle > 1/3$ since $\langle\sigma\rangle = (1/3)\langle g\rangle$. Such a simple lower bound is absent under the ABC. Thus, we can conclude that the boundary-condition dependence of $\langle\sigma\rangle$ is mainly induced by the presence or absence of a perfectly conducting channel.

As demonstrated in Fig. 3, in each of the four cases, the data sets for $\Gamma = 0.6$–4.0 collapse onto one scaling curve upon shifting the data horizontally, where the new length scale a^* is separately determined for each data set. Note that a^* decreases with increasing Γ, playing a role similar to the mean free path. Figure 3 clearly shows that the behaviors of $\langle\sigma\rangle$ in the four cases are different for small L/a^*. However, we observe that the corresponding four curves merge into one scaling curve in the region of $L/a^* \gtrsim 500$. This implies that the scaling curve of $\langle\sigma\rangle$ asymptotically obeys a universal law in the long-length (or strong-disorder) regime of large L/a^*, although it exhibits nonuniversal behavior (i.e., significant dependence on R and the boundary condition) in the short-length (or weak-disorder) regime of small L/a^*.

We also observe that the average conductivity decreases toward a limiting value with decreasing L/a^*. Since $\langle\sigma\rangle$ decreases with decreasing Γ, it is reasonable to identify this limiting value with the conductivity in the clean limit, which is denoted by σ_{cl} hereafter. Note that σ_{cl} does not depend on the system size and is determined by only R and the boundary condition. This follows from the fact that the conductance g_{cl} at the clean limit is analytically given by[46]

$$g_{\mathrm{cl}} = \sum_{m_{\max} \geq |m|} \cosh^{-2}(q_m L) \tag{15}$$

with $q_m L$ being rewritten as $q_m L = 2\pi m R$.[48] Note that the term with $m = 0$, which is allowed only in the PBC case, corresponds to a perfectly conducting channel. We can numerically evaluate σ_{cl} from this expression. The dotted lines in Fig. 3 indicate the resulting values in the four cases. Figure 3 supports the reasoning that $\langle\sigma\rangle$ approaches σ_{cl} with decreasing L/a^* in each case.

Let us consider the behavior of the scaling function β defined by

$$\beta(\langle\sigma\rangle) = \frac{d\ln\langle\sigma\rangle}{d\ln L}. \tag{16}$$

This is determined from the data shown in Fig. 3, and the result for the case with $R = 1$ is shown in Fig. 4. As $\langle\sigma\rangle$ monotonically increases with increasing L/a^*, β is always positive. If $\langle\sigma\rangle$ becomes sufficiently large, we expect that β obeys[12]

$$\beta(\langle\sigma\rangle) = \frac{1}{\pi\langle\sigma\rangle}, \tag{17}$$

in accordance with the weak antilocalization theory.[49] Unfortunately, the regime of such a large $\langle\sigma\rangle$ is not examined in this study owing to the limitation of the computing time. In the opposite regime of $\langle\sigma\rangle$ close to σ_{cl}, β becomes small because the rate of increase in $\langle\sigma\rangle$ is strongly suppressed near the clean limit. Precisely at the clean limit where $\langle\sigma\rangle = \sigma_{\mathrm{cl}}$, β vanishes since σ_{cl} is independent of L. We conclude that $\beta(\langle\sigma\rangle)$ is always positive except at the clean limit, which should be identified as an unstable fixed point. The qualitative features of β argued above apply irrespective of R and the boundary condition although the $\langle\sigma\rangle$ dependence of β is strongly modified at small $\langle\sigma\rangle$ if R and the boundary condition are changed. However, β becomes almost independent of them for sufficiently large $\langle\sigma\rangle$. This implies that the universal behavior of Eq. (17) asymptotically manifests

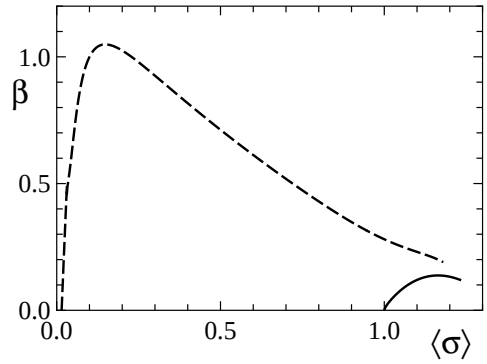

Fig. 4. Scaling function for the case with $R = 1$ determined from the data shown in Fig. 3, where the solid line (dashed line) represents the result under the PBC (ABC).

itself with increasing $\langle\sigma\rangle$.

4. Summary and Discussion

We have studied the conductivity of a 2D Dirac electron system with one Dirac cone in the two-terminal setup, in which the Fermi level is fixed at the Dirac point in the sample region, while the left and right leads are deeply doped. The average conductivity $\langle\sigma\rangle$ is numerically calculated for the system of length L and width W with a fixed aspect ratio $R \equiv L/W$ under the periodic or antiperiodic boundary condition in the transverse direction, where the periodic (antiperiodic) boundary condition directly results in the absence (presence) of a finite-size gap. It is shown that $\langle\sigma\rangle$ monotonically increases with increasing L except at the clean limit, where the conductivity becomes scale-invariant but strongly depends on R and the boundary condition. The scaling function $\beta(\langle\sigma\rangle)$ is determined from the resulting $\langle\sigma\rangle$. The behavior of β is similar to that found in Ref. 10. However, we uncover two features not demonstrated in Ref. 10: the clean limit corresponds to the unstable fixed point at which $\beta(\langle\sigma\rangle)$ vanishes,[14] and $\beta(\langle\sigma\rangle)$ strongly depends on L/W and the boundary condition near the unstable fixed point, although it asymptotically obeys a universal law with increasing $\langle\sigma\rangle$.

The scaling function $\beta(\langle\sigma\rangle)$ has also been determined from the data of $\langle\sigma\rangle$ obtained by a linear response calculation in the momentum space while varying the Fermi level.[12] The resulting $\beta(\langle\sigma\rangle)$ behaves differently from that demonstrated in Fig. 4; it monotonically decreases with increasing $\langle\sigma\rangle$ in accordance with the universal behavior, i.e., Eq. (17). As this calculation treats the system with no electrode away from the Dirac point, the entire setup is completely different from that assumed in the present study. Therefore, we need not seriously consider the difference. However, note that $\beta(\langle\sigma\rangle)$ is not determined in the regime of small $\langle\sigma\rangle$ in Ref. 12. If such a regime were also analyzed within the same approach, its own setup might play a role, resulting in nonuniversal behavior that is different from that demonstrated in Fig. 4. Roughly speaking, Ref. 12 mainly focuses on the universal behavior of $\beta(\langle\sigma\rangle)$, in contrast with that in ordinary 2D electron systems with time-reversal symmetry and strong spin-orbit interaction, while the present study focuses on how $\langle\sigma\rangle$ approaches the universal regime starting from the clean limit under a particular setup.

Acknowledgment

This work was supported by JSPS KAKENHI Grant Number 15K05130.

1) L. Fu, C. L. Kane, and E. J. Mele, Phys. Rev. Lett. **98**, 106803 (2007).
2) J. E. Moore and L. Balents, Phys. Rev. B **75**, 121306 (2007).
3) R. Roy, Phys. Rev. B **79**, 195322 (2009).
4) Y. Ando, J. Phys. Soc. Jpn. **82**, 102001 (2013).
5) N. H. Shon and T. Ando, J. Phys. Soc. Jpn. **67**, 2421 (1998).
6) M. Titov, EPL **79**, 17004 (2007).
7) A. Rycerz, J. Tworzydło, and C. W. J. Beenakker, EPL **79**, 57003 (2007).
8) K. Nomura and A. H. MacDonald, Phys. Rev. Lett. **98**, 076602 (2007).
9) P. M. Ostrovsky, I. V. Gornyi, and A. D. Mirlin, Phys. Rev. Lett. **98**, 256801 (2007).
10) J. H. Bardarson, J. Tworzydło, P. W. Brouwer, and C. W. J. Beenakker, Phys. Rev. Lett. **99**, 106801 (2007).
11) S. Ryu, C. Mudry, H. Obuse, and A. Furusaki, Phys. Rev. Lett. **99**, 116601 (2007).
12) K. Nomura, M. Koshino, and S. Ryu, Phys. Rev. Lett. **99**, 146806 (2007).
13) J. Tworzydło, C. W. Groth, and C. W. J. Beenakker, Phys. Rev. B **78**, 235438 (2008).
14) A. Schuessler, P. M. Ostrovsky, I. V. Gornyi, and A. D. Mirlin, Phys. Rev. B **79**, 075405 (2009).
15) R. Shindou and S. Murakami, Phys. Rev. B **79**, 045321 (2009).
16) P. Goswami and S. Chakravarty, Phys. Rev. Lett. **107**, 196803 (2011).
17) K. Kobayashi, T. Ohtsuki, and K.-I. Imura, Phys. Rev. Lett. **110**, 236803 (2013).
18) K. Kobayashi, T. Ohtsuki, K.-I. Imura, and I. F. Herbut, Phys. Rev. Lett. **112**, 016402 (2014).
19) K. Kobayashi, Y. Yoshimura, K.-I. Imura, and T. Ohtsuki, Phys. Rev. B **92**, 235407 (2015).
20) E. Abrahams, P. W. Anderson, D. C. Licciardello, and T. V. Ramakrishnan, Phys. Rev. Lett. **42**, 673 (1979).
21) S. Hikami, A. I. Larkin, and Y. Nagaoka, Prog. Theor. Phys. **63**, 707 (1980).
22) Y. Asada, K. Slevin, and T. Ohtsuki, Phys. Rev. B **70**, 035115 (2004).
23) P. Markoš and L. Schweitzer, J. Phys. A **39**, 3221 (2006).
24) Y. Zhang, Y. Ran, and A. Vishwanath, Phys. Rev. **79**, 245331 (2009).
25) Y. Zhang and A. Vishwanath, Phys. Rev. Lett. **105**, 206601 (2010).
26) R. Egger, A. Zazunov, and A. Levy Yeyati, Phys. Rev. Lett. **105**, 136403 (2010).
27) J. H. Bardarson, P. W. Brouwer, and J. E. Moore, Phys. Rev. Lett. **105**, 156803 (2010).
28) K.-I. Imura, Y. Takane, and A. Tanaka, Phys. Rev. B **84**, 195406 (2011).

29) T. Ando and T. Nakanishi, J. Phys. Soc. Jpn. **67**, 1704 (1998).
30) T. Ando, T. Nakanishi, and R. Saito, J. Phys. Soc. Jpn. **67**, 2857 (1998).
31) T. Nakanishi and T. Ando, J. Phys. Soc. Jpn. **68**, 561 (1999).
32) T. Ando and H. Suzuura, J. Phys. Soc. Jpn. **71**, 2753 (2002).
33) Y. Takane, J. Phys. Soc. Jpn. **73**, 1430 (2004).
34) Y. Takane, J. Phys. Soc. Jpn. **73**, 2366 (2004).
35) T. Ando, J. Phys. Soc. Jpn. **75**, 054701 (2006).
36) H. Sakai and Y. Takane, J. Phys. Soc. Jpn. **75**, 054711 (2006).
37) M. R. Zirnbauer, Phys. Rev. Lett. **69**, 1584 (1992).
38) Z. Ringel, Y. E. Kraus, and A. Stern, Phys. Rev. B **86**, 045102 (2012).
39) R. S. K. Mong, J. H. Bardarson, and J. E. Moore, Phys. Rev. Lett. **108**, 076804 (2012).
40) H. Obuse, S. Ryu, A. Furusaki, and C. Mudry, Phys. Rev. B **89**, 155315 (2014).
41) Y. Takane, J. Phys. Soc. Jpn. **83**, 103706 (2014).
42) T. Morimoto and A. Furusaki, Phys. Rev. B **89**, 035117 (2014).
43) T. Arita and Y. Takane, J. Phys. Soc. Jpn. **83**, 124716 (2014).
44) K.-I. Imura, M. Okamoto, Y. Yoshimura, Y. Takane, and T. Ohtsuki, Phys. Rev. B **86**, 245436 (2012).
45) Y. Yoshimura, A. Matsumoto, Y. Takane, and K.-I. Imura, Phys. Rev. B **88**, 045408 (2013).
46) M. I. Katsnelson, Eur. Phys. J. B **51**, 157 (2006).
47) H. Tamura and T. Ando, Phys. Rev. B **44**, 1792 (1991).
48) Precisely speaking, the M dependence of the cutoff $m_{\max}$ yields a size dependence of $g_{\rm cl}$. However, it is extremely small and can be safely neglected.
49) H. Suzuura and T. Ando, Phys. Rev. Lett. **89**, 266603 (2002).